

UCLA

UCLA Previously Published Works

Title

Recent progress in $\text{MnBi}_2\text{nTe}_{3\text{n}+1}$ intrinsic magnetic topological insulators: crystal growth, magnetism and chemical disorder.

Permalink

<https://escholarship.org/uc/item/9xg0c17r>

Journal

National Science Review, 11(2)

Authors

Hu, Chaowei

Qian, Tiema

Ni, Ni

Publication Date

2024-02-01

DOI

10.1093/nsr/nwad282

Copyright Information

This work is made available under the terms of a Creative Commons Attribution License, available at <https://creativecommons.org/licenses/by/4.0/>

Peer reviewed

PHYSICS

Special Topic: Recent Progress on the MnBiTe Intrinsic Topological Magnetic Materials

Recent progress in $\text{MnBi}_{2n}\text{Te}_{3n+1}$ intrinsic magnetic topological insulators: crystal growth, magnetism and chemical disorder

Chaowei Hu , Tiema Qian and Ni Ni*

ABSTRACT

The search for magnetic topological materials has been at the forefront of condensed matter research for their potential to host exotic states such as axion insulators, magnetic Weyl semimetals, Chern insulators, etc. To date, the $\text{MnBi}_{2n}\text{Te}_{3n+1}$ family is the only group of materials showcasing van der Waals-layered structures, intrinsic magnetism and non-trivial band topology without trivial bands at the Fermi level. The interplay between magnetism and band topology in this family has led to the proposal of various topological phenomena, including the quantum anomalous Hall effect, quantum spin Hall effect and quantum magnetoelectric effect. Among these, the quantum anomalous Hall effect has been experimentally observed at record-high temperatures, highlighting the unprecedented potential of this family of materials in fundamental science and technological innovation. In this paper, we provide a comprehensive review of the research progress in this intrinsic magnetic topological insulator family, with a focus on single-crystal growth, characterization of chemical disorder, manipulation of magnetism through chemical substitution and external pressure, and important questions that remain to be conclusively answered.

Keywords: MnBi_2Te_4 , magnetic topological insulator, magnetism tuning, antiferromagnetism, ferromagnetism, pressure, chemical doping

Department of Physics
and Astronomy and
California
NanoSystems
Institute, University of
California-Los
Angeles, Los Angeles,
CA 90095, USA

*Corresponding
author. E-mail:
nini@physics.ucla.edu

Received 21 April
2023; Revised 19
August 2023;
Accepted 6
September 2023

INTRODUCTION

The discovery of the magnetic topological insulator MnBi_2Te_4 has been a major advancement in the field of condensed matter physics in its pursuit of the high-temperature quantum anomalous Hall effect (QAHE) [1–5]. A robust quantized Hall resistivity is found at the record high temperature of 1.4 K under a zero field, and even higher temperatures under an external field [4–6], making QAHE much more accessible for its promising applications in low-energy-consumption devices, quantum metrology and quantum computing [7–9]. The report of QAHE in MnBi_2Te_4 follows a decade of precedent works after the discovery of topological insulators. The interplay of non-trivial band topology and magnetic order can lead to numerous novel topological states, such as axion

insulators, magnetic Weyl semimetals, Chern insulators and three-dimensional quantum anomalous Hall (QAH) insulators [10]. This has motivated an intensive ongoing search for materials capable of hosting these proposed states. In 2013, QAHE was first achieved below 90 mK in molecular-beam epitaxy-grown thin films of $\text{Cr}_{0.15}(\text{Bi}_{0.1}\text{Sb}_{0.9})_{1.85}\text{Te}_3$ [11]. The unavoidable magnetic inhomogeneity introduced by magnetic dopants is believed to account for the low critical temperature of the QAHE. Therefore, a magnetic topological insulator (MTI) with intrinsic magnetism is strongly urged. In 2018, MnBi_2Te_4 was discovered as the first van der Waals (vdW) material that features intrinsic magnetism and non-trivial band topology [1–5, 12–25]. It has an A-type antiferromagnetic (AFM) structure where the spins are aligned ferromagnetically in plane and

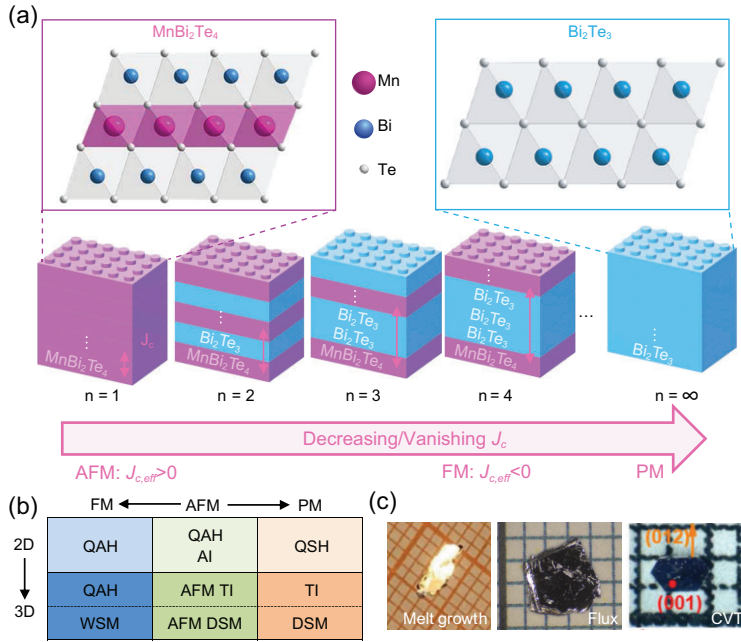


Figure 1. (a) A 'lego set' of MnBi_{2n}Te_{3n+1} and the side view of the [MnBi₂Te₄] SL and [Bi₂Te₃] QL. Purple block: [MnBi₂Te₄] SL. Blue block: [Bi₂Te₃] QL. (b) Rich topological quantum states proposed in MBi₂Te₄ (M = transition/rare-earth metal) in two and three dimensions under different magnetic states from [2]. AI, axion insulator; WSM, Weyl semimetal; DSM, Dirac semimetal. (c) Pictures of single crystals grown from melt growth [57], Bi₂Te₃ flux [15] and CVT [58], respectively.

antiferromagnetically out of plane. Its vdW nature makes possible the exfoliation of the bulk crystal into a thin-film device. As such, one can get even-layer two-dimensional (2D) AFM devices and odd-layer 2D devices with net ferromagnetic (FM) moments. In addition, both angle-resolved photoemission spectroscopy (ARPES) and first-principles density functional theory (DFT) reveal a clean band structure where only the topological surface state appears at the charge neutrality point (CNP) [1,2,20]. Altogether, these unique properties facilitated the rapid realization of QAHE and various other emergent topological states in the MnBi₂Te₄ devices [4–6,26,27].

Following the proposal of MnBi₂Te₄ as an intrinsic MTI, other natural heterostructural members of the MnBi_{2n}Te_{3n+1} ($n \geq 2$) series were discovered [13,25,28–47]. The extension of MnBi₂Te₄ to the greater natural heterostructural MnBi_{2n}Te_{3n+1} family can be seen as a 'lego set' with alternating 'lego pieces' of one MnBi₂Te₄ septuple layer (SL) and ($n - 1$) Bi₂Te₃ quintuple layers (QLs) along the *c* axis, as shown in Fig. 1(a). They are all reported to be intrinsic MTIs with clean band structures near the CNP.

With the natural heterostructure design, various magnetic topological states are theoretically

proposed in MnBi_{2n}Te_{3n+1}. Figure 1(b) summarizes the proposed topological states in MBi₂Te₄ (M = transition/rare-earth metal) [2] depending on the relative strength of spin-orbit coupling and magnetic interactions. Among these topological phases, experimental evidence of Chern insulator and AFM axion insulator states in 2D devices [4–6], as well as AFM TI, PM TI and FM Weyl semimetal states in 3D bulk MnBi₂Te₄ have been observed [48–50]. When the family is extended to MnBi_{2n}Te_{3n+1}, the overall magnetic interaction is weaker, so the magnetic state is more tunable and the topology can be modified accordingly. The AFM members of high-*n* MnBi_{2n}Te_{3n+1} are AFM TIs [28,29,35], whereas the FM members of high-*n* MnBi_{2n}Te_{3n+1} are FM axion insulators where the top and bottom surfaces each contributes half-quantized Hall conductance [30,51]. In addition, the vdW nature of high-*n* MnBi_{2n}Te_{3n+1} also allows the fabrication of new heterostructures that were proposed to give rise to novel topological states, for example, the quantum spin Hall effect with broken time-reversal symmetry in the QL/SL/QL structure [28]. Therefore, this unique natural heterostructural intrinsic MTI series has inspired intensive investigations of their magnetism, band topology, chemical disorder, device functionality, etc.

There are mainly two general ways to obtain MnBi_{2n}Te_{3n+1} flakes: the bottom-up approach that uses molecular-beam epitaxy (MBE) to grow the thin film layer by layer, and the top-down approach that grows single-crystal form and mechanically exfoliates the crystal down to the atomic limit. The MBE allows one to access more metastable phases such as MnBi_{2n}Se_{3n+1} and Mn₄Bi₂Te₇ [52–54] and control local defects, although it is difficult to get rid of the Mn-doped Bi₂Te₃ impurities [55]. The *in situ* measurements such as *in situ* scanning tunneling microscopy (STM) and ARPES allow the study of the band structure, topology and defects without sample degradation that may occur during the device fabrication process [56].

On the other hand, many experimental techniques still require the material in its single-crystal form because a single crystal offers a large volume, well-defined edges and surfaces, crystal orientations, reduced defect levels and uniformity over a large area. The QAHE report was reported in an exfoliated five-layer MnBi₂Te₄ device [4]. Therefore, high-quality single crystals with minimized defects, reduced magnetic inhomogeneity, low carrier density and high mobility are crucial for the studies of MnBi_{2n}Te_{3n+1} and the realization of various emergent phenomena.

Despite rapid advancements in theoretical comprehension and experimental methodologies, research pertaining to $\text{MnBi}_{2n}\text{Te}_{3n+1}$ still faces big challenges. For example, even though quantized Hall conductance has been observed above 8 T in a few groups worldwide, achieving QAHE at zero field has only been realized in one group. Therefore, there exists a pressing need for endeavors to improve crystal growth techniques, enhance device fabrication processes and deepen our understanding of how defects affect magnetism and band topology. These collective efforts are imperative to enhance the success rate of attaining the zero-field QAH state. This review, as an integral component of the Special Topic titled ‘Recent Progress on MnBiTe Intrinsic Topological Magnetic Materials’ will thus be dedicated to crystal growth, chemical disorder and the tuning of magnetism in $\text{MnBi}_{2n}\text{Te}_{3n+1}$. Such understanding will provide fertile ground for designing schemes to realize emergent topological phenomena in this family of materials. The studies can also serve as guidance for future vdW topological magnetic realization based on the key structural ingredients.

THE GROWTH OF HIGH-QUALITY $\text{MnBi}_{2n}\text{Te}_{3n+1}$ SINGLE CRYSTALS

$\text{MnBi}_{2n}\text{Te}_{3n+1}$ is made of alternating SL and QL building blocks, which are depicted in Fig. 1(a). The SL (purple block) consists of a layer of closely packed MnTe_6 octahedra sandwiched between two layers of BiTe_6 octahedra, and they are connected by edge sharing. Each QL (blue block) can be seen as two layers of edge-sharing BiTe_6 octahedra stacked along the c axis. $\text{MnBi}_{2n}\text{Te}_{3n+1}$ with $n = 1$ to $n = \infty$ can be constructed with these SL and QL ‘lego pieces’. The detailed crystal structural stacking rules of $\text{MnBi}_{2n}\text{Te}_{3n+1}$ are elaborated in [30,34].

$\text{MnBi}_{2n}\text{Te}_{3n+1}$ phases can be considered as quasi-metastable. Thus, high-quality single-crystal growth is challenging. The synthesis of $\text{MnBi}_{2n}\text{Te}_{3n+1}$ dates back to the very first discovery of MnBi_2Te_4 in 2013 [12]. Single-crystal growth of MnBi_2Te_4 became extensively studied when it was proposed as an intrinsic MTI in 2018. Today there are mainly three methods of growth to obtain MnBi_2Te_4 single crystals: congruent/incongruent melting, the flux method and the chemical vapor transport method. High- n members ($n \geq 2$) in the $\text{MnBi}_{2n}\text{Te}_{3n+1}$ series can also be grown via similar growth methods, but with much more stringent growth conditions, especially the temperature control. It is noted that sizable phase-pure single crystals have only been made for $n \leq 4$. We next go over each growth technique and discuss the pros and cons as a comparison.

Growth from congruent/incongruent melting

The growth from the melt is done by cooling the stoichiometric melt of the targeted phase through its melting temperature [3,4,13,16,32,35,57,59,60]. Modified Bridgman and vertical Bridgman methods were used. According to the quasi-binary $\text{MnTe}-\text{Bi}_2\text{Te}_3$ phase diagram [13], $\text{MnBi}_{2n}\text{Te}_{3n+1}$ phases crystallize in an 8° temperature window from the incongruent melt. Therefore, an as-grown ingot always has various n phases. Single-crystalline blocks of each phase can be isolated from the as-grown ingot. However, due to the intergrowth, especially on the high- n side, sizable pure-phase single crystals with $n \geq 4$ have not been obtained even using the vertical Bridgman method, which can achieve more precise and consistent temperature control [60]. The mixture is typically heated to around 900°C , where they form a homogeneous liquid. Then it is quickly cooled to 600°C , where the mixture is still MnTe and Bi_2Te_3 . Below 600°C , the $[\text{MnBi}_2\text{Te}_4]$ SL structure starts to be more thermodynamically stable than MnTe , and $\text{MnBi}_{2n}\text{Te}_{3n+1}$ begins to form. To ensure that the process is complete, the mixture needs to be cooled slowly through its melting temperature. It was found that cooling faster than $0.5^\circ\text{C}/\text{h}$ between 600°C and the growth temperature results in excessive Bi_2Te_3 and MnTe [57]. A slow cooling through the solid-liquid phase boundary and prolonged annealing just below the melting temperature are needed, to ensure that the final cooling or the dwelling can last weeks to a month.

In the vertical Bridgman growth, single crystals are grown by gradually moving the stoichiometric melt from the hot zone ($\sim 677^\circ\text{C}$) to the cold zone ($\sim 527^\circ\text{C}$) at a rate of $0.5\text{ mm}/\text{h}$ to cross the melt-solid interface. It requires a larger amount of growth material, but helps to achieve better temperature control in the synthesis. Via this method, despite unavoidable intergrowth for high- n members, one can obtain phases from MnBi_2Te_4 up to $\text{MnBi}_{14}\text{Te}_{22}$ ($n = 7$) from the stoichiometric melt [60]. One can also add MnCl_2 into the growth mixture to provide an Mn-rich environment. Zero-field QAHE is observed at 1.4 K in one piece of MnBi_2Te_4 that was grown with additional MnCl_2 [4].

Growth from the flux method

Flux growth is the method to obtain single crystals out of a high-temperature solution, that is, a flux [61]. Upon cooling, when the solubility of the targeted phase in the flux becomes smaller than the actual concentration, the system becomes over-saturated, and single crystals start to precipitate to lower the concentration in the solution. The crystals nucleate

Table 1. Summary of the chemical, structural and magnetic properties of flux-grown $\text{MnBi}_{2n}\text{Te}_{3n+1}$ from $n = 1$ to 4. Here SJ_1 and SJ_2 refer to the NN and the NNN intraplanar interactions; SJ_c is the NN interplanar interaction; SD is the uniaxial anisotropy energy. The data from high-energy inelastic neutron scattering (INS) measurement are fitted with the J_1 – J_2 model. The data from $M(H)$ are calculated using Equations(2)–(5) below.

	MnBi_2Te_4	MnBi_4Te_7	$\text{MnBi}_6\text{Te}_{10}$	$\text{MnBi}_8\text{Te}_{13}$
n	1	2	3	4
Space group	$R\bar{3}m$	$Pc\bar{3}c$	$R\bar{3}m$	$R\bar{3}m$
Magnetic space group	$R_1\bar{3}c$	$Pc\bar{3}c1$	$R_1\bar{3}c$	$R\bar{3}m'$
Lattice constant a (Å)	4.3336(2) [25]	4.3453(5) [25]	4.361 [34]	4.3749(1) [30]
Lattice constant c (Å)	40.926(3) [25]	23.705(3) [25]	101.300 [34]	132.415(3) [30]
$d_{\text{Mn}} - d_{\text{Te}}$ (Å)	13.642(1)	23.705(3)	33.995(1)	44.138(1)
Mn : Bi : Te (WDS)	0.90 : 2.11 : 4	0.79(2) : 4.29(8) : 7	0.79(1) : 6.30(2) : 10	0.74(3) : 8.2(1) : 13
T_{decant} (°C)	587	585	583	582
Magnetism	AFM	AFM	AFM	FM
T_N/T_C (K)	24	13	11	10.5
H_{sat}^c (T)	7.8	0.22	0.2	0.12
H_{sat}^{ab} (T)	11	1.2	1.2	1.2
SJ_c (meV/Mn) from INS	−0.055 [23]	–	–	–
SJ_1 (meV/Mn) from INS	0.31 [23]	–	–	–
SJ_2 (meV/Mn) from INS	−0.06 [23]	–	–	–
SD (meV/Mn) from INS	0.12 [23]	–	–	–
SJ_c (meV/Mn) from $M(H)$	−0.09 [65,66]	0.0086 [36]	0.0031 [36]	–
SD (meV/Mn) from $M(H)$	0.08 [65,66]	0.098 [36]	0.098 [36]	–
		0.052 [51,74]		

and then continue to grow upon further cooling. For $\text{MnBi}_{2n}\text{Te}_{3n+1}$ growth, Bi_2Te_3 was used as the self-flux, or the solute [15]. Using this growth method, the plate-like single crystals obtained in each batch can be of single phase and sizable phase-pure single crystals have been obtained up to $n = 4$. In the growth, Mn, Bi and Te [15,28–30] are mixed at a ratio of $\text{MnTe} : \text{Bi}_2\text{Te}_3 = x : 100 - x$ with $10 < x < 20$. For high- n $\text{MnBi}_{2n}\text{Te}_{3n+1}$, a lower x is desired to ensure that there is enough flux for the growth. The mixture is placed in an alumina crucible and sealed under a vacuum inside a quartz tube. The ampule was initially heated to 900 °C and held at that temperature for a few hours to ensure a homogeneous liquid. At this stage, the mixture can be considered as MnTe dissolved in Bi_2Te_3 liquid solution. This is followed by a quick cooling to around 600 °C and then a slow cooling down to the targeted decanting temperature T_{decant} (see Table 1 below) in days to weeks. The nucleation rate of MnBi_2Te_4 depends on x and the cooling rate. In general, a smaller x and a slower cooling rate allow for fewer nucleation sites and lead to larger single crystals. After dwelling at T_{decant} for another few days, millimeter-to-centimeter-sized plate-like single crystals can be separated from the liquid flux via a centrifuge.

The key to successful $\text{MnBi}_{2n}\text{Te}_{3n+1}$ flux growth lies in temperature control. The growth is limited by the few-degree temperature window above T_{decant}

where the targeted phase is stable. Therefore, delicate control of the final dwelling temperature T_{decant} is critical. A one-degree offset or less in T_{decant} may result in a different $\text{MnBi}_{2n}\text{Te}_{3n+1}$ phase. Given the temperature sensitivity, careful calibration is needed to determine and access T_{decant} consistently in a box furnace. Usually, a series of test growth runs needs to be done to determine the best temperature profile when a new furnace is in use. This test procedure has been detailed in [30]. In addition to the temperature control by the furnace, one should also keep track of other factors that can cause slight shifts in temperatures, such as the location of the growth ampule in the furnace, the relative vertical position of the material in the growth ampule and the length of the growth ampule to make sure that T_{decant} is repeatedly accessible.

Because T_{decant} is close to the melting point of the flux, a quick spin-out process (less than 5 s) is essential to remove the flux while it remains in its liquid form. Additional means can be taken to delay the solidification of the liquid flux. These methods include increasing the quantity of starting materials, preheating the ampule container of the centrifuge and incorporating extra layers of thermal insulation for the quartz ampule. For instance, applying the silver paste on the quartz walls or enclosing the growth ampule within a larger-diameter quartz tube can help enhance the insulating properties of the ampule.

Lastly, in flux growth, the flux is often embedded inside the targeted crystals. Indeed, unavoidable Bi_2Te_3 -phase impurities can be found inside the targeted $\text{MnBi}_{2n}\text{Te}_{3n+1}$ phase grown by the flux method. X-ray diffractions (XRDs) can be used to carefully screen out the pieces with minimal embedded flux to ensure accurate measurements of their physical properties.

Growth from the chemical vapor transport method

Chemical vapor transport (CVT) is a method that has been widely adopted to grow single crystals of vdW materials such as transition-metal chalcogenides. So far, single-crystal MnBi_2Te_4 and MnBi_4Te_7 can be grown this way. The growth involves a gaseous transport agent that can form intermediate volatile compounds with the constituting elements of the targeted material at the source end. Then at the sink side, which is the cold end for most reactions, the intermediate gaseous phases dissociate, condensing into the targeted phase and forming single crystals over time. For the growth of the $\text{MnBi}_{2n}\text{Te}_{3n+1}$ family, I_2 , TeI_4 and BiI_3 have been used as the transport agent [58,62]. In all cases, MnI_2 becomes the dominant iodide species during the growth, and the concentration of the intermediate gaseous phase is limited by the volatility of MnI_2 , so there is no qualitative difference between these transport agents [62]. Alternatively, one can use chlorides such as MnCl_2 , TeCl_4 and MoCl_5 as transport agents. However, the transport with chloride is less efficient because MnCl_2 and other intermediate chloride phases are less volatile than their iodide counterparts, so the transport rate is limited by the lower vapor pressure of MnCl_2 , resulting in smaller crystals [62].

Given the metastability of the $\text{MnBi}_{2n}\text{Te}_{3n+1}$ phase, it is unsurprising that $\text{MnBi}_{2n}\text{Te}_{3n+1}$ growth with vapor requires delicate control of the temperature too. Considerations are as follows. Firstly, the sink-end temperature should be well tested. The maximum temperature of the cold end should not exceed the melting point of $\text{MnBi}_{2n}\text{Te}_{3n+1}$, or the condensed phase will be in liquid form; moreover, at a higher temperature near 600°C , MnBi_2Te_4 is no longer stable and thus Bi_2Te_3 droplets and MnTe single crystals will appear. Secondly, if the cold-end temperature is too low, the growth will be limited by an insufficient Mn transport rate, so only Bi_2Te_3 forms. So, if a near-stoichiometric mixture is used as the source material, the cold-end temperature can be chosen to be T_{decant} [58]. But, if it is in the Mn-rich condition, the MnBi_2Te_4 phase can form over

a range of cold-end temperatures and suppress the formation of high- n members of $\text{MnBi}_{2n}\text{Te}_{3n+1}$ as well as Mn-doped Bi_2Te_3 [62]. Thirdly, the temperature gradient should be small, in the range $3\text{--}20\text{ K}$ so that the cold-end temperature is more stable and the transport rate is not too high.

The CVT growth of $\text{MnBi}_{2n}\text{Te}_{3n+1}$ can be done in a box furnace, where the temperature is overall uniform and well controlled with a small intrinsic temperature gradient either vertically from top to bottom, horizontally from side to middle or from the middle to the furnace door. This is sufficient to drive transport growth. When a tube furnace is used, a careful calibration of the temperature at the hot and cold ends is necessary to ensure that the temperature condition is met to obtain the targeted phase.

A representative image from each growth is included in Fig. 1(c). The CVT-grown samples are typically millimeter sized and marked with well-defined hexagonal edges, (001) and (012) planes. In comparison, the crystal is less well defined when grown from the stoichiometric melt. The samples grown with flux are usually large in size with as-grown ab planes, but their edges are not well defined. Therefore, the unique growth habit of CVT-grown samples provides opportunities for in-plane and side surface measurements. In addition, the CVT crystals also tend to be Bi_2Te_3 -free and Mn richer than flux growth for both MnBi_2Te_4 [58] and MnSb_2Te_4 [62], which may be beneficial for QAHE realization, as we discuss in the section entitled ‘Disorder: antisites and optimization’.

Growth of chemically doped $\text{MnBi}_{2n}\text{Te}_{3n+1}$

Single-crystal series with Sb doping on the Bi sites, or Sn and Pb doping on the Mn sites have been made. There is no Se doping on the Te sites reported. The difficulty in obtaining the bulk form with Se doping stems from the fact that bulk MnBi_2Se_4 is only reported in the monoclinic ($C2/m$) non-vdW phase and only thin-film MnBi_2Se_4 grown by MBE shares the same structure as MnBi_2Te_4 [54].

The three growth methods for $\text{MnBi}_{2n}\text{Te}_{3n+1}$ can all be generalized to their isostructural non-magnetic sister compounds (Sn, Pb) $(\text{Bi, Sb})_{2n}\text{Te}_{3n+1}$, and the chemically doped systems that exist continuously in between. In the flux growth of the Sb-doping series, since the melting point of Sb_2Te_3 is $\sim 35^\circ$ higher than that of Bi_2Te_3 [63], the decanting temperature must be correspondingly increased to be slightly higher than the melting point of $(\text{Bi}_{1-x}\text{Sb}_x)_2\text{Te}_3$, which increases with x . As a result, the optimal growth window is reduced. It

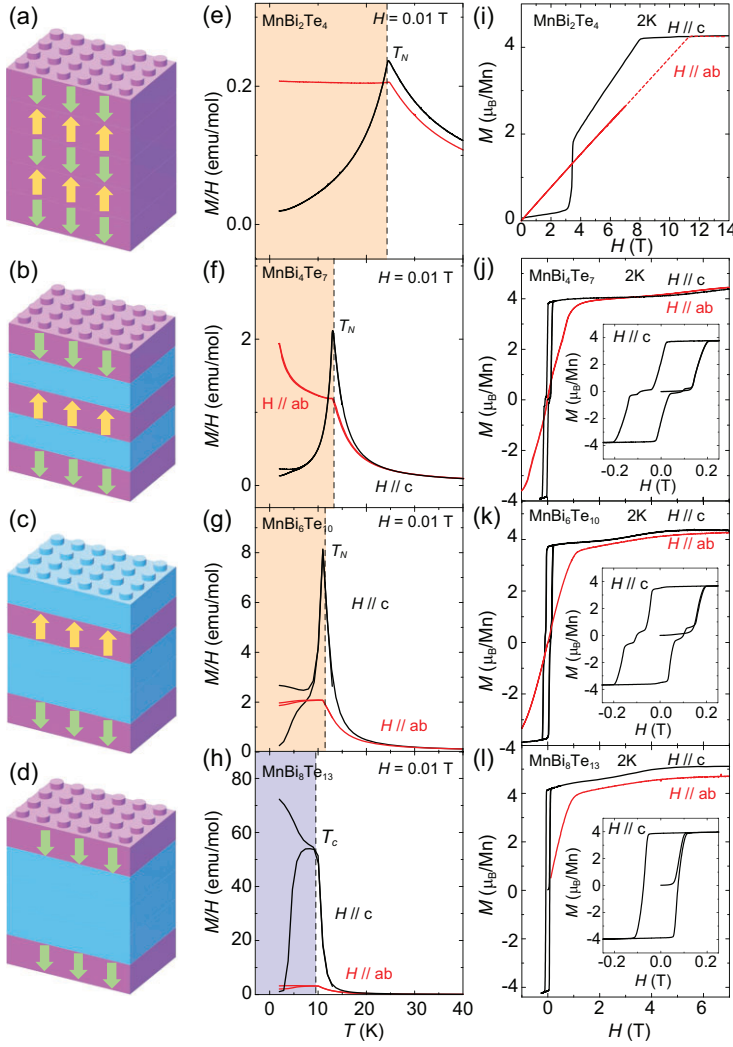


Figure 2. Magnetism of $\text{MnBi}_{2n}\text{Te}_{3n+1}$. (a–d) Magnetic structure for MnBi_2Te_4 , MnBi_4Te_7 , $\text{MnBi}_6\text{Te}_{10}$ and $\text{MnBi}_8\text{Te}_{13}$, respectively. (e–h) The temperature-dependent magnetic susceptibility measured with in-plane and out-of-plane magnetic fields. (i–l) Isothermal magnetization under in-plane and out-of-plane fields at 2 K. Insets of (j–l): the magnetization hysteresis loop near zero field. Figures are reproduced from [20,28,30,58].

was also found that the actual doping levels are slightly higher in flux growth than the nominal ratio [51].

When growing $(\text{Mn}/\text{X})\text{Bi}_{2n}\text{Te}_{3n+1}$ by flux ($\text{X} = \text{Sn}, \text{Pb}$), adjustment of the synthesis condition is needed depending on the shift of the eutectic point between the $(\text{Mn}/\text{X})\text{Bi}_{2n}\text{Te}_{3n+1}$ and Bi_2Te_3 fluxes. For flux growth of $(\text{Mn}_{1-x}\text{Sn}_x)\text{Bi}_2\text{Te}_4$, the $(\text{Mn}_{1-x}\text{Sn}_x)\text{Te} : \text{Bi}_2\text{Te}_3$ ratio and temperature profile remain the same for x up to 66% [64]. However, for flux growth of the Pb-doping series, although the temperature profile remains the same, a higher $(\text{Mn}_{1-x}\text{Pb}_x)\text{Te} : \text{Bi}_2\text{Te}_3$ ratio is found to be critical for the successful flux growth when higher x is involved [65], likely because PbTe dissolves more easily in Bi_2Te_3 than MnTe and SnTe. In such a case,

a series of test growth runs is necessary to locate the eutectic point and determine the optimal ratio and temperatures.

EVOLUTION OF MAGNETISM IN $\text{MnBi}_{2n}\text{Te}_{3n+1}$

$\text{MnBi}_{2n}\text{Te}_{3n+1}$ compounds with Mn^{2+} ($S = 5/2$) ions offer an excellent and tunable platform for studying vdW magnetism since they all share the same building block for magnetism—the Mn layer in the middle of the SL, with varying interlayer coupling strengths. Table 1 summarizes the key parameters of their magnetic order and interactions. As shown in Fig. 2(a)–(d), within each SL, the FM Mn-Te-Mn superexchange interactions overwhelmingly win the AFM-preferred Mn-Mn direct interactions and result in an in-plane FM configuration. In MnBi_2Te_4 , the interlayer coupling is AFM, which results in the A-type easy-axis antiferromagnetic structure. By increasing the number of Bi_2Te_3 spacer layers, the spacing between Mn-Mn layers and the superexchange path between them are effectively increased. Therefore, the AFM coupling is weakened and eventually becomes weaker than other mechanisms for FM coupling such as dipolar interactions, and antisite-mediated exchange, so the magnetism becomes FM along the c axis, as demonstrated by the magnetic properties summarized in Fig. 2(e)–(h). For those with an A-type AFM, when an external magnetic field H is applied along the easy c axis, a spin-flop transition appears in MnBi_2Te_4 , and spin-flip transitions are observed in MnBi_4Te_7 and $\text{MnBi}_6\text{Te}_{10}$, as summarized in Fig. 2(i)–(l).

Such evolution of magnetism under an external magnetic field can be captured by the Hamiltonian for the magnetic ground state, as shown in

$$E = - \sum_{i,i'} J_1 \mathbf{S}_i \cdot \mathbf{S}_{i'} - \sum_{i,i'} J_2 \mathbf{S}_i \cdot \mathbf{S}_{i'} - \sum_{ij} J_c \mathbf{S}_i \cdot \mathbf{S}_j - \sum_i D S_{iz}^2 - \sum_i g \mu_B \mathbf{H} \cdot \mathbf{S}_{i,z}. \quad (1)$$

The terms include strong FM intraplanar exchange coupling (dominated by J_1 and J_2 for the nearest neighbor (NN) and next-nearest neighbor (NNN), respectively), weak NN Mn-Mn interplanar coupling J_c , magnetic anisotropy D that can generally be absorbed into the single-site term and Zeeman energy when an external magnetic field is present. Here, interactions beyond the NNN are omitted. We denote by i, i' sites in the same SL, and by i, j sites in the neighboring SL; $D > 0$ is for our 2D easy-axis system, while $D < 0$ stands for the easy-plane anisotropy.

The evolution of magnetism results from the competition between the J_c term, D term and the Zeeman term. Equation (1) can thereby be simplified into the bilayer Stoner–Wohlfarth model by only considering these three terms. By this [23,65,66], SD and SJ_c can be estimated as

$$|SD| = (H_{sf}^2/H_s^{//c})(g\mu_B/2), \quad (2)$$

$$|SJ_c| = (g\mu_B/2z)(H_{sf}^2/H_s^c + H_s^c). \quad (3)$$

Here z is the number of NN Mn of an Mn ion, which is 6 for $n = 1, 3, 4$ and 2 for $n = 2$. We denote by H_{sf} the spin-flop field and by $H_s^{//c}$ the saturation field with $H//c$. We can also obtain SD and SJ_c by

$$|SD| = (H_s^{//ab} - H_s^{//c})(g\mu_B/4), \quad (4)$$

$$|SJ_c| = (H_s^{//ab} + H_s^{//c})(g\mu_B/4z). \quad (5)$$

Here $H_s^{//ab}$ denotes the saturation field with $H//ab$. The spin gap can be estimated as $\Delta = 2SD\sqrt{zSJ_c/SD + 1}$.

By such, experimental estimations of SJ_c and SD from the $M(H)$ data for $\text{MnBi}_{2n}\text{Te}_{3n+1}$ ($n \leq 3$) are summarized in Table 1. Meanwhile, SJ_c , SJ_1 , SJ_2 and SD determined from inelastic neutron scattering (INS) are also summarized in Table 1. The values obtained from these two methods agree with each other in magnitude. Among all $\text{MnBi}_{2n}\text{Te}_{3n+1}$, MnBi_2Te_4 has the strongest interlayer exchange, and the ratio of $|J_c/J_1|$ measured by INS is ~ 0.18 [23]. The ratio is expected to be much lower for other $\text{MnBi}_{2n}\text{Te}_{3n+1}$ that have much smaller $|J_c|$ but comparable $|J_1|$ within the SL. The small $|J_c/J_1|$ is unsurprising considering their long interlayer Mn-Mn superexchange path, which ranges from 13.642 Å in MnBi_2Te_4 to 44.1 Å in $\text{MnBi}_8\text{Te}_{13}$. This leads to a much weaker interlayer exchange interaction than the intralayer ones and thus quasi-2D magnetism.

From $n = 1$ to 3, J and D are generally of the same order of magnitude in SL, while J_c decreases the most and affects the magnetic behavior the most. Firstly, a 2D easy-axis system with $D > 0$ orders at a general temperature of

$$T_c = \frac{a|J|}{b + \log(|J/J_{\text{eff}}|)}, \quad (6)$$

where a and b are constants of the order of 1, and J_{eff} is a combination of J_c and D that reduces to D in the $J_c \rightarrow 0$ limit [67]. Since MnBi_2Te_4 has the strongest J_c and thus J_{eff} , according to Equation (6), it has the highest T_c of 24 K. The temperature T_c quickly decreases to 13 K in MnBi_4Te_7

and then slowly decreases to 10.5 K in $\text{MnBi}_8\text{Te}_{13}$ since J_{eff} reduces to $\sim D$ in these high- n members. Secondly, in MnBi_2Te_4 , the ratio of $|J_c/D| \sim 0.45$ suggests the comparable J_c and D here and thus a weak anisotropy scenario. The competition between J_c , D and the Zeeman term leads to a spin-flop transition as the three terms prefer the spins in opposite configurations, along the easy c axis and along the field direction, respectively. Together, a canted AFM state that minimizes the overall energy is favored in the intermediate field regime [17]. On the other hand, in MnBi_4Te_7 and $\text{MnBi}_6\text{Te}_{10}$ where $|D/J_c|$ is much larger, the system exhibits strong anisotropy and thus undergoes a spin-flip transition. Thirdly, as a result of smaller J_c , the saturation field in MnBi_4Te_7 and $\text{MnBi}_6\text{Te}_{10}$ is 40 times smaller than that in MnBi_2Te_4 . The minor step at 0.1 T for $\text{MnBi}_6\text{Te}_{10}$ is possibly due to some FM domain formations and it has been universally observed in $\text{MnBi}_6\text{Te}_{10}$ [29,32,36]. Lastly, with $H//ab$, the much reduced J_c in high- n members also leads to a 10 times smaller saturation field of 1.2 T than 11 T in MnBi_2Te_4 .

Eventually, at $n = 4$, $\text{MnBi}_{2n}\text{Te}_{3n+1}$ becomes an axion ferromagnet that shows long-range FM ordering at 10.5 K with clear FM hysteresis at 2 K. Relaxation behaviors are observed. One scenario to understand this relaxation is to look at $\text{MnBi}_8\text{Te}_{13}$ as a truly 2D magnet with independent FM planes, the so-called ‘single-layer magnetism’, a 2D planar analog of the more commonly known single-molecule magnet [68], which should give rise to spin-glass-like magnetic relaxation behavior. An alternative scenario is the conventional ferromagnet picture that attributes the relaxation behavior to the irreversible FM domain movements [69]. Indeed, relaxation behavior was also reported in the AC susceptibility in Sb-doped MnBi_4Te_7 and $\text{MnBi}_6\text{Te}_{10}$ as well as in ferromagnetic MnSb_2Te_4 [68–71]. Furthermore, the vanishing interlayer magnetic interactions lead to the low formation energy of the magnetic domain boundary and thus very soft FM domains here. As a result, rare ‘double-peak’ behavior is observed in the AC susceptibility under small DC bias fields [69].

It is worth noting that, for MnBi_4Te_7 and $\text{MnBi}_6\text{Te}_{10}$ with different growth methods or growth conditions, FM ground states were also observed [70,72]. The disparities are likely attributed to varying degrees of crystal defects within samples grown by different groups, which we discuss extensively in the next section.

Another important feature of magnetism in $\text{MnBi}_{2n}\text{Te}_{3n+1}$ is the robust in-plane FM fluctuations that tend to persist above the ordering temperatures and may induce the Zeeman gap for the QAHE

realization [73]. High-frequency or high-field electron spin resonance (HF-ESR) spectroscopy reveals a zero-field FM excitation gap of 0.11 meV up to 30 K in MnBi_4Te_7 [74]. Although the zero-field AFM gap of 0.45 meV in MnBi_2Te_4 closes at T_N , HF ESR finds FM-type spin fluctuations above T_N in MnBi_2Te_4 at magnetic fields above 6 T. Hence, it is the generic property of the SLs that short-range FM spin correlations persist far above the ordering temperature, provided that the SLs are decoupled either by spacer layers or moderate magnetic fields. Spatially varied magnetic fluctuations were also imaged by nitrogen-vacancy relaxometry in MnBi_4Te_7 nanoflakes above its ordering temperature [75].

DISORDER: ANTISITES AND OPTIMIZATION

Although the Chern insulator state can be observed in the polarized FM state of MnBi_2Te_4 under high magnetic fields even above $T_N = 24$ K [6], the zero-field QAHE was only reported below the critical temperature $T_{\text{QAHE}} = 1.4$ K in a five-layer device [4]. At zero field, the magnetic inhomogeneity arising from the chemical disorder reduces the universal magnetism-induced surface gap. This reduction in the gap prevents the achievement of the QAHE at higher temperatures. Therefore, to have a high success rate in realizing QAHE and an enhanced ratio of T_{QAHE}/T_N in an MnBi_2Te_4 device, understanding and controlling its defects is essential.

The typical defects in $\text{MnBi}_{2n}\text{Te}_{3n+1}$ include antisite defects, vacancies and stacking faults [76]. They have played an important role in the magnetism and band topology in the $\text{MnBi}_{2n}\text{Te}_{3n+1}$ family. For example, in the case of $\text{MnBi}_6\text{Te}_{10}$, an FM state can be achieved by having additional Mn vacancies in the sample [72]. In addition to these defects in the bulk samples, when the crystals are exfoliated and fabricated into devices, the fabrication process can introduce defects too. For example, the synergistic interaction between the Mn-Bi antisite defects and Te deficiency induced by traces of oxygen in the fabrication environment may promote surface reconstruction [77]. In this review, we focus only on the defects in bulk crystals.

Scanning transmission electron microscopy (STEM), STM, X-ray and neutron diffractions, and magnetization analysis have identified and quantified the chemical defects in $\text{MnBi}_{2n}\text{Te}_{3n+1}$ [15,16,23,25,34,51,58,72,78–84]. Each technique has its pros and cons. For example, STEM and STM can directly visualize the defects, but quantitative analysis of defect concentration is hard with

STEM because the image is an average of the overall slab, and STM is only surface sensitive; diffraction techniques are bulk measurements, but the refined results depend on the structural model used; the magnetization analysis is only sensitive to the magnetic elements and requires high magnetic fields to polarize the spins. Therefore, as complementary techniques, it is beneficial to compare the results of these techniques. The topographic STM imaging directly visualizes the antisite defects on the cleaved (001) surface [15,78]. It reveals predominant Mn_{Bi} (Mn substitution of Bi atoms on the Bi site) and minor Bi_{Te} (Bi substitution of Te atoms on the Te site) antisite disorders. Bi_{Te} makes up around 0.2% of Te sites in MnBi_2Te_4 , while Mn_{Bi} accounts for 3% of Bi sites in flux-grown MnBi_2Te_4 crystals [15,78] and 5% in congruent-melting-grown MnBi_2Te_4 [79]. This is not surprising since compared to congruent-melting growth, the flux growth contains stoichiometrically less Mn in the starting materials. Similar defect patterns were commonly observed in the STM images of Mn-doped Bi_2Te_3 , and also in the QL of MnBi_4Te_7 [80,81]. For MnBi_4Te_7 , the amount of Mn_{Bi} is suggested to be 2.1% in the SL and 3% in the QL [80].

XRD or neutron diffraction provides an indirect route to obtain defect concentrations, which may depend on the structural model used for the refinement. Since the neutron scattering lengths of Mn and Bi have opposite signs, neutron diffraction is unique in resolving the occupancy of Mn and Bi on each site. In MnBi_2Te_4 grown via the congruent-melting growth, XRD refinement was performed [16,79]. The refinement was carried out using a charge neutrality constraint and a structural model that allowed for Mn-Bi antisite disorder and Mn vacancies, while Te was assumed to occupy full occupancy on Te sites. The results suggest that 21.5(1)% Bi_{Mn} , 5.7(1)% Mn_{Bi} and 4.9(1)% of Mn sites are voids [16], resulting in $\text{Mn}_{0.85(3)}\text{Bi}_{2.10(3)}\text{Te}_4$. If the vacancies are not included in the refinement, the percentages for Bi_{Mn} and Mn_{Bi} become 17.5% and 8.8% [79], which will lead to a stoichiometry inconsistent with the chemical analysis. In a flux-grown MnBi_2Te_4 studied by single-crystal neutron scattering that assumes full occupancy of Te, 18(1)% of Mn is occupied by Bi in MnBi_2Te_4 and only a negligible amount of 1(1)% Bi sites are occupied by Mn [25], leading to $\text{Mn}_{0.84}\text{Bi}_{2.16}\text{Te}_4$. The single-crystal neutron measurement also suggests that the Bi_{Mn} percentages are 27.9(4)%, 34(1)% and 36(4)% for MnBi_4Te_7 , $\text{MnBi}_6\text{Te}_{10}$ and $\text{MnBi}_8\text{Te}_{13}$ respectively, with an amount of Mn_{Bi} that is below the measurement resolution of neutron scattering [25,34].

Isothermal magnetization analysis provides one more way to estimate the small amount of Mn

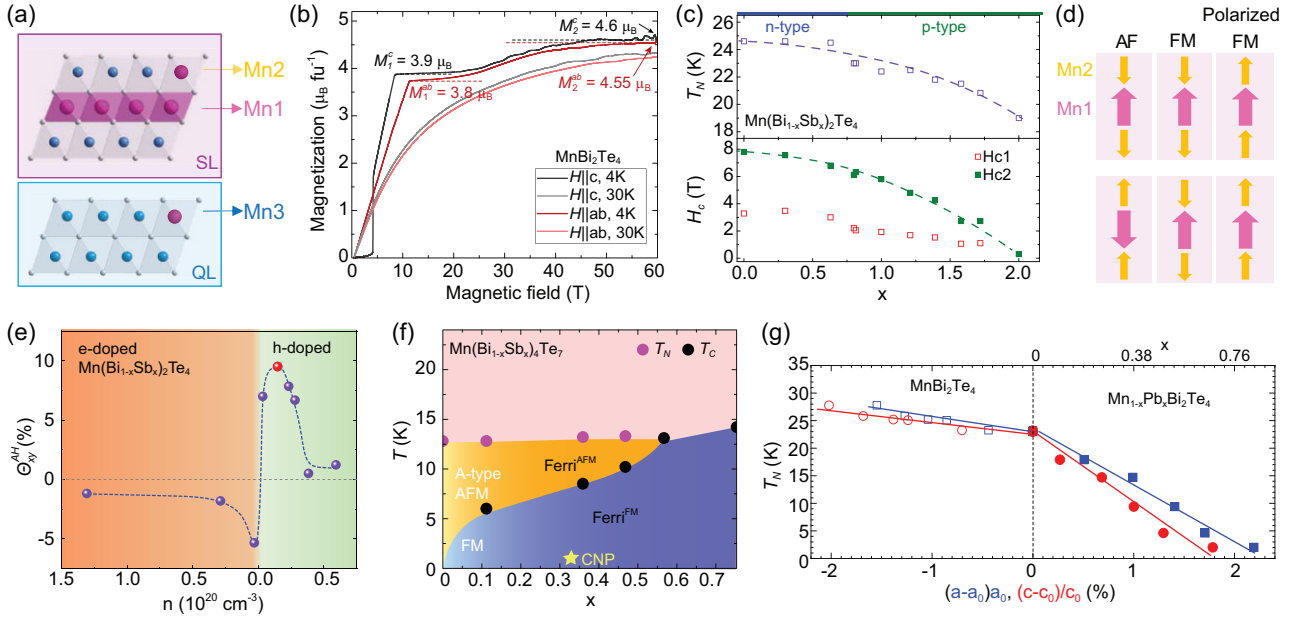


Figure 3. Antisite defects and the effect of Sb doping in MnBi_2Te_4 and MnBi_4Te_7 . (a) Mn1 (Mn_{Mn}), Mn2 (Mn_{Bi} in the $[\text{MnBi}_2\text{Te}_4]$ SL) and Mn3 (Mn_{Bi} in the $[\text{Bi}_2\text{Te}_3]$ QL). (b) Isothermal magnetization $M(H)$ in MnBi_2Te_4 up to 60 T for $H||c$ and $H||ab$ [83]. (c) The doping dependence of the ordering temperature T_N - x and saturation fields H_c - x of $\text{Mn}(\text{Bi}_{1-x}\text{Sb}_x)_2\text{Te}_4$ grown by flux [66]. (d) The evolution of the magnetic structure of $\text{Mn}(\text{Bi}_{1-x}\text{Sb}_x)_2\text{Te}_4$ under high field. AFM represents the magnetism of an AFM-like ground state. FM represents the magnetism of an FM-like ground state. Polarized FM represents the magnetism when all Mn moments are polarized at 50 T [83]. (e) The anomalous Hall conductivity with carrier concentration [48] in FM MnBi_2Te_4 , consistent with the proposed type-II Weyl nodes. (f) The T - x phase diagram of $\text{Mn}(\text{Bi}_{1-x}\text{Sb}_x)_4\text{Te}_7$ [51]. (g) Temperature T_N versus the lattice parameter change in MnBi_2Te_4 under external pressure [87] and Pb doping [65].

antisites. In [83], a method for estimating the antisite concentration was developed for MnBi_2Te_4 based on knowledge of the magnetic structure and its evolution under magnetic fields. Here, to better distinguish the Mn sites, we denote the Mn_{Mn} as Mn1 and the Mn_{Bi} as Mn2, as shown in Fig. 3(a). Here Mn1 concentrations are affected by Mn_{Bi} as well as Mn vacancies. In MnBi_2Te_4 , each Mn sublattice is an A-type AFM, while Mn2 spins are strongly AFM coupled to Mn1 spins. Lai *et al.* [83] found that in the $M(H)$ curve of MnBi_2Te_4 , besides the spin-flop transition and saturation at 7.8 T, as shown in Fig. 2(i), one more metamagnetic transition was observed with a plateau around 50 T, as shown in Fig. 3(b). The intriguing $M(H)$ can be understood as follows. At 7.8 T, an individual Mn1 or Mn2 sublattice enters their polarized FM state, while Mn1 and Mn2 are still strongly AFM coupled; it takes 50 T to make Mn2 spins FM aligned with the Mn1 spins [83]. Therefore, $M(7.8 \text{ T}) \propto n_{\text{Mn1}} - 2n_{\text{Mn2}}$ and $M(50 \text{ T}) \propto n_{\text{Mn1}} + 2n_{\text{Mn2}}$. By this, n_{Mn1} and n_{Mn2} , the respective concentrations of Mn1 and Mn2, are estimated to be 83.5% and 3.2% in the flux-grown sample, whereas in the CVT-grown sample, they are estimated to be 87.4% and 3.8% [58]. The method has also been used to estimate the antisite amount in MnBi_4Te_7 where there are more metamagnetic plateaus due to

the additional Mn3 site (Mn_{Bi} in Bi_2Te_3 QL) [51], as shown in Fig. 3(a). By this method, the Mn1, Mn2 and Mn3 concentrations are estimated as 73%, 1.5% and 3% in MnBi_4Te_7 [51], which are consistent with the STM measurements [80].

While defect formation during crystal growth is entropy driven and therefore inevitable, there are also internal structural factors that further promote the dominant antisite defects. It is argued that the internal strain of the MnTe layer is responsible for the high density of Bi_{Mn} defects, and its low formation energy was confirmed by DFT [85]. Compared to that in pure MnTe with in-plane lattice constant $a = 4.15 \text{ \AA}$, the Mn layer in MnBi_2Te_4 is stretched to $a = 4.31 \text{ \AA}$. Given the small atomic size of Mn, it is energetically favorable to form Mn vacancies and for large Bi atoms to enter to relieve the strain in the Mn layer, resulting in the overall decrease of the Mn1 concentration. As n increases, the lattice parameter a of the MnBi_2Te_4 layer is brought closer to Bi_2Te_3 in order to form a stable natural heterostructure, resulting in $a \sim 4.37 \text{ \AA}$ in high- n $\text{MnBi}_{2n}\text{Te}_{3n+1}$, so more Bi_{Mn} have to enter to relieve the strain on the Mn layer. Indeed, via neutron diffraction, Bi_{Mn} is found to increase from 18(1)% in MnBi_2Te_4 to 36(4)% in $\text{MnBi}_8\text{Te}_{13}$ [25,34]. Meanwhile, an opposite compressive effect is present but milder in the Bi

layer since $a \sim 4.40 \text{ \AA}$ in Bi_2Te_3 , so Mn_{Bi} will happen too but at a lesser extent, varying from 1(1)% to 3% of the Bi sites in flux-grown MnBi_2Te_4 crystals [15,78] and 4-5% in congruent-melting and CVT-grown samples [58,79]. Thus, overall, MnBi_2Te_4 appears Mn deficient. The same is happening in high- n members with slightly smaller Mn_{Bi} , as suggested by the analysis of the isothermal magnetization and neutron diffraction [51,72].

Since Bi_{Mn} and Mn_{Bi} are correlated negatively, we may only choose to optimize one or the other. For device application and the search for QAHE, it is important to understand the roles of Mn_{Bi} and Bi_{Mn} . Mn1 provides the major source of magnetism in the material, so Bi_{Mn} results in inhomogeneous Zeeman fields and reduces the associated Dirac gap in the surface states. In addition, one Bi_{Mn} donates an additional electron to the system, which brings in the spatial variation of the Fermi level and further reduces the global surface state gap. On the other hand, Mn_{Bi} weakens the overall effective Zeeman field in the system and acts as an electron acceptor, and the effect is inhomogeneous too.

Ways to tune defects include varying growth conditions, growth methods and chemical doping. In general, slower cooling and additional thermal annealing are two common routes to ensure thermodynamic equilibrium during the growth and give more uniform single crystals. Meanwhile, reducing the antisite formations remains an active topic in the crystal growth of this family of compounds. Growth efforts have shown that, for the flux-grown and CVT-grown samples, the analysis of the isothermal magnetization data revealed that the Bi_{Mn} percentages are 16.5% (flux grown) and 12.6% (CVT grown) and that the Mn_{Bi} percentages are 3.2% (flux grown) and 3.8% (CVT grown) [58]. Therefore, growing crystals in an Mn-rich environment indeed increases the Mn occupancy on the Mn site that is good for the realization of the QAHE; this, however, also slightly increases Mn_{Bi} , which is detrimental to the QAHE. Calculation of the defect formation energy also suggests that Mn_{Bi} can be minimized in a Te-rich condition [85]. For growth from melting, temperature control can be critical for affecting the overall Mn level: FM $\text{MnBi}_6\text{Te}_{10}$ is grown at a temperature 5° higher than that for AFM $\text{MnBi}_6\text{Te}_{10}$. It is found that the FM sample contains more Mn vacancies than the AFM samples, and overall Mn levels are lower [72]. Chemical doping provides another route to change the free energy of formation for different defect types. For example, Sb substitution of Bi leads to more Mn_{Bi} antisites, which we discuss more extensively in the next section.

The defects are also nontrivial in the aspect of topology. In ARPES, there have been discrepant reports on the Dirac point being slightly gapped or gapless in the surface states of MnBi_2Te_4 . It was shown that the AFM-coupled Mn2 antisites can greatly reduce the Dirac point gap size locally [56,86]. It is also found that CVT-grown MnBi_2Te_4 , which has more Mn1 and Mn2, is favorable to consistently achieving a quantized Hall resistance at high field [58]. The underlying picture could be that Mn1 increases much more than Mn2, leading to an overall spatially more homogeneous magnetization. Therefore, increasing the total Mn in crystal growth may benefit the realization of quantized Hall resistance.

For high- n $\text{MnBi}_{2n}\text{Te}_{3n+1}$ systems, although the interlayer FM state becomes more accessible with a larger n , the amount of Mn1 also decreases, making the sample more electron doped. As a result, it is difficult to tune the device to the CNP and the device studies are so far much more limited.

THE EFFECT OF CHEMICAL DOPING

The as-grown $\text{MnBi}_{2n}\text{Te}_{3n+1}$ is heavily electron doped. ARPES measurement shows that the CNP of $\text{MnBi}_{2n}\text{Te}_{3n+1}$ is located 0.24–0.4 eV below the Fermi level, much larger than the bulk or surface gap [20–22,24,28,30,45]. Therefore, the transport properties arising from the topological features are screened by the electron conduction from the bulk. This hinders access to the topological states and motivates studies to lower the Fermi energy through Sb doping. Since Sb has a relatively closer electronegativity and ionic radius to Mn compared to Bi, substitution of Bi with Sb significantly increases the amount of $\text{Mn}_{\text{Bi/Sb}}$, which adds holes in the system and makes the charge carriers go from electron type to hole type. However, the additional magnetic sublattice arising from the increased $\text{Mn}_{\text{Bi/Sb}}$ antisites also results in complex magnetism [19,51,66,70,88,89].

According to Yan *et al.* [66], $\text{Mn}(\text{Bi}_{1-x}\text{Sb}_x)_2\text{Te}_4$ remains AFM for the whole doping range, T_N and the spin-flop and saturation fields monotonically decrease with x , as presented in the T - x and H - x phase diagrams in Fig. 3(c). However, at higher x , drastically different magnetic ground states are found in different literature, with some showing FM behavior and some remaining AFM [66,82,90–94]. Neutron scattering measurement on one AFM and one FM MnSb_2Te_4 sample distinguished the underlying difference [82]. As shown in Fig. 3(d), in both samples, Mn1 and Mn2 sublattices are antiferromagnetically coupled to each other [82,90]. In the one that shows AFM behavior, an individual Mn1 or Mn2

sublattice is A-type AFM, while in the other one that shows FM behavior, an Mn1 or Mn2 sublattice is individually FM. This ferrimagnetic nature leads to a reduced magnetic moment at 7 T observed in experiments. The actual composition is determined to be $\text{Mn}_{0.588}\text{Sb}_{0.412}(\text{Sb}_{0.871}\text{Mn}_{0.129})_2\text{Te}_4$ for the former and $\text{Mn}_{0.635}\text{Sb}_{0.365}(\text{Sb}_{0.850}\text{Mn}_{0.150})_2\text{Te}_4$ for the latter, indicating the existence of a critical level of Mn2 that can switch the interlayer interaction of Mn1 from AFM to FM. In practice, the defect concentration can be delicately controlled with slightly different temperature profile, starting material from the growth [82] and growth method [62].

Sb doping adds holes to the system since Mn_{Sb} (electron acceptors) formation is more energetically favorable than $(\text{Sb})_{\text{Mn}}$ (electron donors) [85]. Indeed, the charge carrier density evolves linearly with doping and a cross-over from electron to hole behavior is found near $x = 0.315$ in MnBi_2Te_4 [19,66]. The trend was also directly identified via ARPES [19], where the Fermi level is tuned near the Dirac point around the nominal concentration of $x = 0.3$. The control of the chemical potential with Sb doping thus allows one to access and study the topological states by transport measurements. For example, a recent report shows that devices fabricated with flux-grown $\text{Mn}(\text{Bi}_{1-x}\text{Sb}_x)_2\text{Te}_4$ single crystal have quantized Hall resistance above 6 T [95]. In particular, the effect is achieved near zero gating near the CNP. The capability of tuning the chemical potential via Sb doping also enables one to map the band structure via quantum oscillations to search for new topological states. In the bulk form, FM MnBi_2Te_4 is proposed to be a clean type-II Weyl semimetal [1,2]. Because the FM can only be achieved under high field, which limits the use of other band structure measurement techniques such as ARPES, quantum oscillation is the right tool here. One way quantum oscillation is commonly used for this purpose is by extracting the Berry phase from the Lifshitz-Kosevich fitting. However, because the system is intrinsically time-reversal-symmetry breaking, the extracted phase factor is not guaranteed to be π or 0 [96,97]. Given its clean band structure, one can in principle map out the exact evolution of electron and hole pockets near the CNP, and then compare it with the DFT calculations to try to confirm the type-II Weyl band structure [48,97]. The result is that the extracted frequency and effective mass from the quantum oscillation are consistent with the DFT calculation [97]. More recently, a signature intermediate state where both electron and hole pockets coexist has been reported by Jiang *et al.* [50], who provided direct evidence of the type-II Weyl nodes. Meanwhile, there is other transport evidence

supporting the type-II Weyl semimetal state. One observation is the negative longitudinal magnetoresistance due to a chiral anomaly [48]. However, one needs to distinguish the effect of a chiral anomaly and suppressed magnetic scattering at high fields. The chiral anomaly occurs when $\mathbf{E} \parallel \mathbf{B}$, so the negative magnetoresistance (MR) under the magnetic field caused by the chiral anomaly is strongly angular dependent, while negative MR induced by spin scattering is independent of the field direction. The recent angular-dependent measurements in [49] show that the negative MR in Sb-doped MnBi_2Te_4 is consistent with the chiral anomaly expected for the Weyl states. The other signature of type-II Weyl states is the sharp mobility peak and diverging anomalous Hall conductance that flips sign at the CNP, as shown in Fig. 3(e) [48,50,98], contrasting a type-I Weyl semimetal whose anomalous Hall conductance would remain constant across the CNP.

For MnBi_4Te_7 systems [51], the CNP is at $x = 0.36$. The switching of the magnetism on the Mn1 sublattice is continuously controlled in $\text{Mn}(\text{Bi}_{1-x}\text{Sb}_x)_4\text{Te}_7$. Here, besides Mn1 and Mn2, an additional Mn3 (Mn_{Bi} in the QL) sublattice exists (see Fig. 3(a)). The interlayer exchange interaction of Mn1 is the result of the competition between the superexchange interaction bridged by the nonmagnetic Bi/Sb/Te anions and the exchange interaction mediated by Mn3. The former favors AFM here and the latter always favors FM. When Sb is doped, Mn1 decreases, while Mn2, Mn3 and total Mn concentrations increase [51]. Therefore, upon increasing x , the Mn3-assisted FM interaction becomes stronger and wins. Upon cooling, since the Mn3-assisted interaction follows the Curie-Weiss law and the superexchange interaction is weakly temperature dependent for a 2D system, FM interaction wins at lower temperatures. This scenario explains the $T-x$ phase diagram shown in Fig. 3(f). By varying the growth condition, it is possible to obtain different anisotropy levels, leading to some seemingly controversial observations. For example, FM Mn1-Mn1 interlayer interaction can dominate even in pure MnBi_4Te_7 at low temperatures and lower Sb dopings, while AFM Mn1-Mn1 interlayer interaction can also appear in MnSb_4Te_7 [70,88,99]. Such delicate magnetic interaction in this system allows versatile means to easily trigger metamagnetic transitions, as we will see in the next section. Similarly, FM Mn1-Mn1 interaction can be achieved in $\text{Mn}(\text{Bi}_{1-x}\text{Sb}_x)_6\text{Te}_{10}$ at even smaller doping [68,89].

When the Mn site is substituted by X ($X = \text{Sn/Pb}$) [64,65], the main effect is the dilution of the Mn sublattice. This effectively modifies the Hamiltonian of the energy scheme in $(\text{Mn}_{1-x}\text{X}_x)\text{Bi}_2\text{Te}_4$ by introducing an additional factor of $\delta = 1 - x$

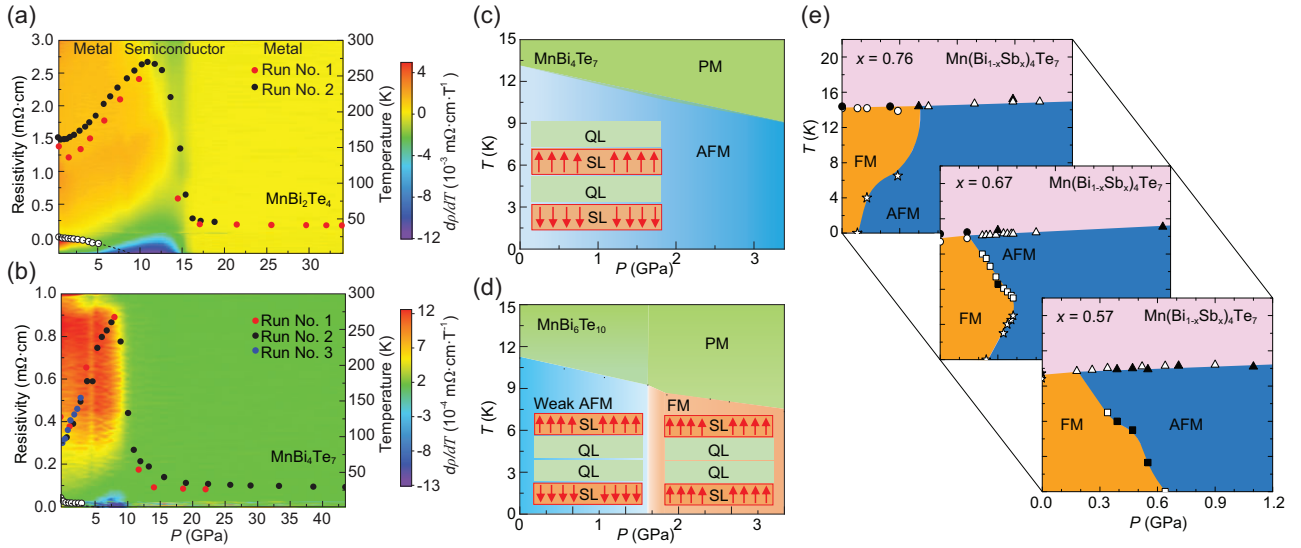


Figure 4. The temperature-pressure (T – P) phase diagrams of $\text{MnBi}_{2n}\text{Te}_{3n+1}$. (a and b) The T – P phase diagrams of MnBi_2Te_4 and MnBi_4Te_7 , respectively, up to ~ 40 GPa. Filled circles represent different runs of resistivity measurements at 1.8 K and open circles indicate AFM transition temperatures obtained from transport measurement [100]. (c and d) The T – P phase diagrams of MnBi_4Te_7 and $\text{MnBi}_6\text{Te}_{10}$ up to ~ 3 GPa, respectively [101]. (e) The T – P phase diagrams of $\text{Mn}(\text{Bi}_{1-x}\text{Sb}_x)_4\text{Te}_7$ below 1.2 GPa. Filled and open data points are obtained from transport and magnetization measurements, respectively [67].

on the effective spin of the Mn/X site [65], leading to the linear decrease of T_N with x , as shown in Fig. 3(g). X doping also changes the distribution of antisite defects. For example, the refinement of the neutron diffraction data on the $(\text{Mn}_{0.55(4)}\text{Pb}_{0.33(4)})\text{Bi}_{2.10(2)}\text{Te}_4$ single crystal will not converge if Mn_{Bi} is present. In this case, the minimization of Mn_{Bi} could be a result of the Mn-lesser environment and an increase in lattice parameter a upon Pb doping. Consequently, the electron carrier density increases with doping. The reduction of Mn_{Bi} makes X doping a promising tuning parameter to optimize Mn1 and Mn2 in MnBi_2Te_4 crystals for the realization of QAHE.

TUNING THE GROUND STATES BY EXTERNAL PRESSURE

External pressure offers a continuous tuning parameter of the system in a clean and non-intrusive way. By compressing the lattice and thereby modifying the interaction strength and band structure, it can serve as a powerful tool in tuning the ground state and topological properties. The high-pressure study has been carried out among $\text{MnBi}_{2n}\text{Te}_{3n+1}$ and its extended material family. Figure 4 summarizes a few selected pressure phase diagrams.

The pressure measurements of MnBi_2Te_4 were conducted up to tens of gigapascals [87,100]. As shown in Fig. 4(a), there is a complete suppression of T_N at around 9 GPa. The resistivity at 1.8 K, ρ

(1.8 K), first increases slightly with pressure, then undergoes a sharp drop around 15 GPa, where XRD suggests that it enters an amorphous state and the vdW gap vanishes [100]. MnBi_4Te_7 remains overall metallic in the transport measurement with a reduction in resistivity above 10 GPa in Fig. 4(b), and XRD suggests a structural transition to a monoclinic phase at 15.9 GPa and then a cubic phase at 18.6 GPa with no observation of an amorphous phase [100]. A closer examination below 3.5 GPa shows an almost linear decrease of T_N [100,101] and an increase in the saturation field with pressure, shown in Fig. 4(c). DFT calculations suggest that, when external pressure compresses the lattice, it increases the interlayer exchange interaction, leading to the increased saturation field according to Equation (5), while it also weakens the intralayer FM coupling, leading to the decreased T_N according to Equation (6) [101]. In $\text{MnBi}_6\text{Te}_{10}$ where the interlayer coupling is even weaker, both T_N and the saturation field decrease with pressure (Fig. 4(d)), suggesting an accompanying decrease in the interlayer and intralayer couplings in this system. Surprisingly, when pressure exceeds 1.2 GPa, the overall Mn1–Mn1 interlayer interaction switches from AFM to FM. The authors argue that this is because the nearly vanishing interlayer AFM coupling is suppressed by the stronger FM intralayer fluctuations [101].

Pressure-driven metamagnetic transitions were observed in $\text{Mn}(\text{Bi}_{1-x}\text{Sb}_x)_4\text{Te}_7$ [67]. Here, external pressure fine-tuned the already-delicate

FM and AFM energy scales, resulting in distinct temperature-pressure phase diagrams for different x (Fig. 4(e)). The magnetic ordering temperature (upper phase line) remains little changed under pressure. According to Equation (6), the ordering temperature depends logarithmically weakly on the ratio J/J_{eff} and is thus weakly pressure dependent. On the other hand, the metamagnetic transition temperature T_M phase line (the lower phase line) is unconventional. It is very sensitive to the pressure and temperature, and varies with doping: $dT_M/dP < 0$ for $x \lesssim 0.6$, $dT_M/dP > 0$ for $x \gtrsim 0.7$; in particular, dT_M/dP is positive at low temperatures and negative at higher temperatures for $x = 0.67$, showing an AFM-FM-AFM re-entrance behavior upon cooling. These unconventional lower phase lines arise from the competition between the superexchange Mn1-Mn1 AFM interaction and the Mn3-assisted FM Mn1-Mn1 interaction that we discussed in the previous section. Since the strength of the Mn3-assisted FM interaction is proportional to the susceptibility of Mn3, upon cooling, such a competition can result in an AFM-FM transition at small Mn3 concentrations, an AFM-FM-AFM transition at intermediate Mn3 concentrations and an FM-AFM transition at higher Mn3 concentrations. This leads to the observed T - P phase diagram across different doping regions [67].

The effect of pressure was measured in MnSb_2Te_4 [102] and MnSb_4Te_7 [103] up to 40 and 80 GPa, respectively. The temperature T_N was suppressed under pressure and structural phase transitions were observed. MnSb_2Te_4 enters into an amorphous-like phase above 16.6 GPa, while MnSb_4Te_7 goes from trigonal $P\bar{3}m1$ to monoclinic $C2/m$ at 16.2 GPa and then to a simple cubic $Im\bar{3}m$ phase at 25.7 GPa. In particular, a superconducting state emerges at 30 GPa in MnSb_4Te_7 [103], which maxes out at 50.7 GPa with a critical temperature of 2.2 K. This is the first report of superconductivity in the series, but it appears in the high-pressure cubic phase instead of the vdW trigonal $P\bar{3}m1$ phase.

OUTLOOKS

$\text{MnBi}_{2n}\text{Te}_{3n+1}$ and its extended family provide a material platform with excellent tunability in structure, magnetism and band topology. The compatibility between the non-magnetic QL and the magnetic SL leads to the $\text{MnBi}_{2n}\text{Te}_{3n+1}$ series where the magnetism evolves from a strongly interlayer coupled A-type AFM TI at $n = 1$, to a weakly interlayer coupled A-type AFM TI at $n = 2, 3$ and to an FM axion insulator at $n \geq 4$. Moreover, magnetism in these systems can be fine-tuned through lattice modulations and defect redistribution. In the weak interlayer in-

teraction limit especially, the magnetism of this material family can be manipulated by growth conditions, chemical doping and external pressure. Combined with the non-trivial topological properties of the materials, the versatile magnetism opens up the possibility of realizing emergent phenomena including QAHE, QSHE, etc.

To realize the exotic states predicted in $\text{MnBi}_{2n}\text{Te}_{3n+1}$, sustained efforts are needed to produce high-quality single crystals. As defects are inevitable, defect engineering is necessary to fine-tune and locate optimal defect distributions, which could be the key to increasing the success rate of the realization of QAHE. Such tuning can be done by varying growth conditions, including synthesis methods, growth temperature, time, chemical environment and post-annealing effect. We have seen that Sb or Pb doping indeed modified antisite formation. In addition, Na doping on the Mn site was predicted to be an effective doping that only reduces Bi_{Mn} [82], which awaits experimental verification. It also remains an open question if single-crystal growth under high pressure can make the SL and QL a better lattice match to reduce the number of antisites.

The general material design principles of natural heterostructural $\text{MnBi}_{2n}\text{Te}_{3n+1}$ are not limited to this material family. Knowledge of the growth of metastable phases, understanding the effect of defects in magnetism and topology, etc. have flourished with the tremendous efforts in studies of natural heterostructural materials. The research in this aspect can serve as a guide to growing more intrinsic magnetic topological materials. Examples include $\text{Mn}_n\text{Bi}_2\text{Te}_{3+n}$, where more than one MnTe layer is embedded within each slab, was proposed [104] and observed in thin-film growth for $n = 3$ [53]. Recently, $\text{Mn}_2\text{Bi}_2\text{Te}_5$ has also been identified [62,105] in the bulk sample, although it only comes in as a small amount of impurity phase of MnBi_2Te_4 . This entails, by now unsurprisingly, more delicate metastable magnetic topological insulator phases awaiting us to explore. Ongoing research is needed to continue optimizing $\text{MnBi}_{2n}\text{Te}_{3n+1}$ and search for more MTI candidates to provide a fertile ground for the interplay between topology and magnetism and the realization of QAHE at higher temperatures with good reproducibility.

FUNDING

Work at UCLA was supported by the U.S. Department of Energy (DOE), Office of Science, Office of Basic Energy Sciences under Award DE-SC0021117.

Conflict of interest statement. None declared.

REFERENCES

1. Zhang D, Shi M and Zhu T *et al.* Topological axion states in the magnetic insulator MnBi_2Te_4 with the quantized magnetoelectric effect. *Phys Rev Lett* 2019; **122**: 206401.
2. Li J, Li Y and Du S *et al.* Intrinsic magnetic topological insulators in van der Waals layered MnBi_2Te_4 -family materials. *Sci Adv* 2019; **5**: eaaw5685.
3. Otrokov MM, Klimovskikh II and Bentmann H *et al.* Prediction and observation of an antiferromagnetic topological insulator. *Nature* 2019; **576**: 416–22.
4. Deng Y, Yu Y and Shi MZ *et al.* Quantum anomalous Hall effect in intrinsic magnetic topological insulator MnBi_2Te_4 . *Science* 2020; **367**: 895–900.
5. Liu C, Wang Y and Li H *et al.* Robust axion insulator and chern insulator phases in a two-dimensional antiferromagnetic topological insulator. *Nat Mater* 2020; **19**: 522–7.
6. Ge J, Liu Y and Li J *et al.* High-Chern-number and high-temperature quantum Hall effect without Landau levels. *Natl Sci Rev* 2020; **7**: 1280–7.
7. He K, Wang Y and Xue QK. Topological materials: quantum anomalous Hall system. *Annu Rev Condens Matter Phys* 2018; **9**: 329–44.
8. Liu CX, Zhang SC and Qi XL. The quantum anomalous Hall effect: theory and experiment. *Annu Rev Condens Matter Phys* 2016; **7**: 301–21.
9. Wang J, Lian B and Qi XL *et al.* Quantized topological magnetoelectric effect of the zero-plateau quantum anomalous Hall state. *Phys Rev B* 2015; **92**: 081107.
10. Tokura Y, Yasuda K and Tsukazaki A. Magnetic topological insulators. *Nat Rev Phys* 2019; **1**: 126–43.
11. Chang CZ, Zhang J and Feng X *et al.* Experimental observation of the quantum anomalous Hall effect in a magnetic topological insulator. *Science* 2013; **340**: 167–70.
12. Lee DS, Kim TH and Park CH *et al.* Crystal structure, properties and nanostructuring of a new layered chalcogenide semiconductor, Bi_2MnTe_4 . *CrystEngComm* 2013; **15**: 5532–8.
13. Aliev ZS, Amirasanov IR and Nasonova DI *et al.* Novel ternary layered manganese bismuth tellurides of the $\text{MnTe-Bi}_2\text{Te}_3$ system: synthesis and crystal structure. *J Alloys Compd* 2019; **789**: 443–50.
14. Gong Y, Guo J and Li J *et al.* Experimental realization of an intrinsic magnetic topological insulator. *Chin Phys Lett* 2019; **36**: 076801.
15. Yan JQ, Zhang Q and Heitmann T *et al.* Crystal growth and magnetic structure of MnBi_2Te_4 . *Phys Rev Mater* 2019; **3**: 064202.
16. Zeugner A, Nietschke F and Wolter AU *et al.* Chemical aspects of the candidate antiferromagnetic topological insulator MnBi_2Te_4 . *Chem Mater* 2019; **31**: 2795–806.
17. Lee SH, Zhu Y and Wang Y *et al.* Spin scattering and noncollinear spin structure-induced intrinsic anomalous Hall effect in antiferromagnetic topological insulator MnBi_2Te_4 . *Phys Rev Res* 2019; **1**: 012011.
18. Otrokov MM, Rusinov IP and Blanco-Rey M *et al.* Unique thickness-dependent properties of the van der Waals interlayer antiferromagnet MnBi_2Te_4 films. *Phys Rev Lett* 2019; **122**: 107202.
19. Chen B, Fei F and Zhang D *et al.* Intrinsic magnetic topological insulator phases in the Sb doped MnBi_2Te_4 bulks and thin flakes. *Nat Commun* 2019; **10**: 1–8.
20. Hao YJ, Liu P and Feng Y *et al.* Gapless surface dirac cone in antiferromagnetic topological insulator MnBi_2Te_4 . *Phys Rev X* 2019; **9**: 041038.
21. Chen Y, Xu L and Li J *et al.* Topological electronic structure and its temperature evolution in antiferromagnetic topological insulator MnBi_2Te_4 . *Phys Rev X* 2019; **9**: 041040.
22. Li H, Gao SY and Duan SF *et al.* Dirac surface states in intrinsic magnetic topological insulators EuSn_2As_2 and $\text{MnBi}_{2n}\text{Te}_{3n+1}$. *Phys Rev X* 2019; **9**: 041039.
23. Li B, Yan JQ and Pajeroski DM *et al.* Competing magnetic interactions in the antiferromagnetic topological insulator MnBi_2Te_4 . *Phys Rev Lett* 2020; **124**: 167204.
24. Li H, Liu S and Liu C *et al.* Antiferromagnetic topological insulator MnBi_2Te_4 : synthesis and magnetic properties. *Phys Chem Chem Phys* 2020; **22**: 556–63.
25. Ding L, Hu C and Ye F *et al.* Crystal and magnetic structures of magnetic topological insulators MnBi_2Te_4 and MnBi_4Te_7 . *Phys Rev B* 2020; **101**: 020412.
26. Gao A, Liu YF and Hu C *et al.* Layer Hall effect in a 2D topological axion antiferromagnet. *Nature* 2021; **595**: 521–5.
27. Ovchinnikov D, Huang X and Lin Z *et al.* Intertwined topological and magnetic orders in atomically thin Chern insulator MnBi_2Te_4 . *Nano Lett* 2021; **21**: 2544–50.
28. Hu C, Gordon KN and Liu P *et al.* A van der Waals antiferromagnetic topological insulator with weak interlayer magnetic coupling. *Nat Commun* 2020; **11**: 97.
29. Tian S, Gao S and Nie S *et al.* Magnetic topological insulator $\text{MnBi}_6\text{Te}_{10}$ with a zero-field ferromagnetic state and gapped dirac surface states. *Phys Rev B* 2020; **102**: 035144.
30. Hu C, Ding L and Gordon KN *et al.* Realization of an intrinsic ferromagnetic topological state in $\text{MnBi}_6\text{Te}_{13}$. *Sci Adv* 2020; **6**: eaba4275.
31. Deng H, Chen Z and Woloś A *et al.* High-temperature quantum anomalous Hall regime in a $\text{MnBi}_2\text{Te}_4/\text{Bi}_2\text{Te}_3$ superlattice. *Nat Phys* 2021; **17**: 36–42.
32. Shi M, Lei B and Zhu C *et al.* Magnetic and transport properties in the magnetic topological insulators $\text{MnBi}_2\text{Te}_4(\text{Bi}_2\text{Te}_3)_n$ ($n = 1, 2$). *Phys Rev B* 2019; **100**: 155144.
33. Sun H, Xia B and Chen Z *et al.* Rational design principles of the quantum anomalous Hall effect in superlattice-like magnetic topological insulators. *Phys Rev Lett* 2019; **123**: 096401.
34. Ding L, Hu C and Feng E *et al.* Neutron diffraction study of magnetism in van der Waals layered $\text{MnBi}_{2n}\text{Te}_{3n+1}$. *J Phys D* 2021; **54**: 174003.
35. Wu J, Liu F and Sasase M *et al.* Natural van der Waals heterostructural single crystals with both magnetic and topological properties. *Sci Adv* 2019; **5**: eaax9989.
36. Yan JQ, Liu Y and Parker D *et al.* A-type antiferromagnetic order in MnBi_4Te_7 and $\text{MnBi}_6\text{Te}_{10}$ single crystals. *Phys Rev Mater* 2020; **4**: 054202.
37. Gordon KN, Sun H and Hu C *et al.* Strongly gapped topological surface states on protected surfaces of antiferromagnetic MnBi_4Te_7 and $\text{MnBi}_6\text{Te}_{10}$. *arXiv*, 2019. <https://arxiv.org/abs/1910.13943>
38. Souchay D, Nentwig M and Günther D *et al.* Layered manganese bismuth tellurides with GeBi_4Te_7 - and $\text{GeBi}_6\text{Te}_{10}$ -type structures: towards multifunctional materials. *J Mater Chem C* 2019; **7**: 9939–53.
39. Hu Y, Xu L and Shi M *et al.* Universal gapless Dirac cone and tunable topological states in $(\text{MnBi}_2\text{Te}_4)_m(\text{Bi}_2\text{Te}_3)_n$ heterostructures. *Phys Rev B* 2020; **101**: 161113.
40. Xu L, Mao Y and Wang H *et al.* Persistent surface states with diminishing gap in $\text{MnBi}_2\text{Te}_4/\text{Bi}_2\text{Te}_3$ superlattice antiferromagnetic topological insulator. *Sci Bull* 2020; **65**: 2086–93.
41. Jo NH, Wang LL and Slager RJ *et al.* Intrinsic axion insulating behavior in antiferromagnetic $\text{MnBi}_6\text{Te}_{10}$. *Phys Rev B* 2020; **102**: 045130.
42. Rienks E, Wimmer S and Sánchez Barriga J *et al.* Large magnetic gap at the Dirac point in $\text{Bi}_2\text{Te}_3/\text{MnBi}_2\text{Te}_4$ heterostructures. *Nature* 2019; **576**: 423–8.
43. Tan A, Labracherie V and Kunchur N *et al.* Metamagnetism of weakly coupled antiferromagnetic topological insulators. *Phys Rev Lett* 2020; **124**: 197201.
44. Klimovskikh II, Otrokov MM and Estyunin D *et al.* Tunable 3D/2D magnetism in the $(\text{MnBi}_2\text{Te}_4)(\text{Bi}_2\text{Te}_3)_m$ topological insulators family. *npj Quantum Mater* 2020; **5**: 1–9.

45. Vidal R, Bentmann H and Facio J *et al.* Orbital complexity in intrinsic magnetic topological insulators MnBi_4Te_7 and $\text{MnBi}_6\text{Te}_{10}$. *Phys Rev Lett* 2021; **126**: 176403.
46. Lu R, Sun H and Kumar S *et al.* Half-magnetic topological insulator with magnetization-induced Dirac gap at a selected surface. *Phys Rev X* 2021; **11**: 011039.
47. Zhong H, Bao C and Wang H *et al.* Light-tunable surface state and hybridization gap in magnetic topological insulator $\text{MnBi}_6\text{Te}_{13}$. *Nano Lett* 2021; **21**: 6080–6.
48. Lee SH, Graf D and Min L *et al.* Evidence for a magnetic-field-induced ideal type-II Weyl state in antiferromagnetic topological insulator $\text{Mn}(\text{Bi}_{1-x}\text{Sb}_x)_2\text{Te}_4$. *Phys Rev X* 2021; **11**: 031032.
49. Lee SH, Graf D and Robinson R *et al.* Evidence of magnetic fluctuation induced Weyl semimetal state in the antiferromagnetic topological insulator $\text{Mn}(\text{Bi}_{1-x}\text{Sb}_x)_2\text{Te}_4$. *Phys Rev B* 2023; **107**: 205105.
50. Jiang Q, Palmstrom JC and Singleton J *et al.* Fermi surface evolution and anomalous Hall effect in an ideal type-II Weyl semimetal, arXiv, 2023. <https://arxiv.org/abs/2306.08339>
51. Hu C, Lien SW and Feng E *et al.* Tuning magnetism and band topology through antisite defects in Sb-doped MnBi_4Te_7 . *Phys Rev B* 2021; **104**: 054422.
52. Hirahara T, Ereemeev SV and Shirasawa T *et al.* Large-gap magnetic topological heterostructure formed by subsurface incorporation of a ferromagnetic layer. *Nano Lett* 2017; **17**: 3493–500.
53. Hirahara T, Otrokov MM and Sasaki T *et al.* Fabrication of a novel magnetic topological heterostructure and temperature evolution of its massive Dirac cone. *Nat Commun* 2020; **11**: 4821.
54. Zhu T, Bishop AJ and Zhou T *et al.* Synthesis, magnetic properties, and electronic structure of magnetic topological insulator MnBi_2Se_4 . *Nano Lett* 2021; **21**: 5083–90.
55. Zhao YF, Zhou LJ and Wang F *et al.* Even–odd layer-dependent anomalous Hall effect in topological magnet MnBi_2Te_4 thin films. *Nano Lett* 2021; **21**: 7691–8.
56. Liu M, Lei C and Kim H *et al.* Visualizing the interplay of Dirac mass gap and magnetism at nanoscale in intrinsic magnetic topological insulators. *Proc Natl Acad Sci USA* 2022; **119**: e2207681119.
57. Yu S, Zhao K and Yang X *et al.* The synthesis of MnBi_2Te_4 antiferromagnetic topological insulator single crystals through a one-step growth method. *J Supercond Nov Magn* 2022; **35**: 1221–8.
58. Hu C, Gao A and Berggren BS *et al.* Growth, characterization, and Chern insulator state in MnBi_2Te_4 via the chemical vapor transport method. *Phys Rev Mater* 2021; **5**: 124206.
59. Cui J, Shi M and Wang H *et al.* Transport properties of thin flakes of the antiferromagnetic topological insulator MnBi_2Te_4 . *Phys Rev B* 2019; **99**: 155125.
60. Amiraslanov I, Aliev Z and Askerova P *et al.* Crystal structure and Raman-active lattice vibrations of magnetic topological insulators MnBi_2Te_4 - $n(\text{Bi}_2\text{Te}_3)$ ($n = 0, 1, \dots, 6$). *Phys Rev B* 2022; **106**: 184108.
61. Canfield PC and Fisk Z. Growth of single crystals from metallic fluxes. *Philos Mag B* 1992; **65**: 1117–23.
62. Yan JQ, Huang Z and Wu W *et al.* Vapor transport growth of MnBi_2Te_4 and related compounds. *J Alloys Compd* 2022; **906**: 164327.
63. Orujlu E, Aliev Z and Amiraslanov I *et al.* Phase equilibria of the MnTe–Sb₂Te₃ system and synthesis of novel ternary layered compound– MnSb_4Te_7 . *Phys Chem Solid State* 2021; **22**: 39–44.
64. Zhu J, Naveed M and Chen B *et al.* Magnetic and electrical transport study of the antiferromagnetic topological insulator Sn-doped MnBi_2Te_4 . *Phys Rev B* 2021; **103**: 144407.
65. Qian T, Yao YT and Hu C *et al.* Magnetic dilution effect and topological phase transitions in $(\text{Mn}_{1-x}\text{Pb}_x)\text{Bi}_2\text{Te}_4$. *Phys Rev B* 2022; **106**: 045121.
66. Yan JQ, Okamoto S and McGuire MA *et al.* Evolution of structural, magnetic, and transport properties in $\text{MnBi}_{2-x}\text{Sb}_x\text{Te}_4$. *Phys Rev B* 2019; **100**: 104409.
67. Qian T, Emmanouilidou E and Hu C *et al.* Unconventional pressure-driven metamagnetic transitions in topological van der Waals magnets. *Nano Lett* 2022; **22**: 5523–9.
68. Wu J, Liu F and Liu C *et al.* Toward 2D magnets in the $(\text{MnBi}_2\text{Te}_4)(\text{Bi}_2\text{Te}_3)_n$ bulk crystal. *Adv Mater* 2020; **32**: 2001815.
69. Hu C, Tanatar MA and Prozorov R *et al.* Unusual dynamic susceptibility arising from soft ferromagnetic domains in $\text{MnBi}_6\text{Te}_{13}$ and Sb-doped $\text{MnBi}_{2n}\text{Te}_{3n+1}$ ($n = 2, 3$). *J Phys D* 2021; **55**: 054003.
70. Guan YD, Yan CH and Lee SH *et al.* Ferromagnetic MnBi_4Te_7 obtained with low-concentration Sb doping: a promising platform for exploring topological quantum states. *Phys Rev Mater* 2022; **6**: 054203.
71. Li H, Li Y and Lian Y *et al.* Glassy magnetic ground state in layered compound MnSb_2Te_4 . *Sci China Mater* 2022; **65**: 477–85.
72. Yan C, Zhu Y and Miao L *et al.* Delicate ferromagnetism in $\text{MnBi}_6\text{Te}_{10}$. *Nano Lett* 2022; **22**: 9815–22.
73. Scholten M, Facio JI and Ray R *et al.* Finite temperature fluctuation-induced order and responses in magnetic topological insulators. *Phys Rev Res* 2021; **3**: L032014.
74. Alfonsov A, Mehlawat K and Zeugner A *et al.* Magnetic-field tuning of the spin dynamics in the magnetic topological insulators $(\text{MnBi}_2\text{Te}_4)(\text{Bi}_2\text{Te}_3)_n$. *Phys Rev B* 2021; **104**: 195139.
75. McLaughlin NJ, Hu C and Huang M *et al.* Quantum imaging of magnetic phase transitions and spin fluctuations in intrinsic magnetic topological nanoflakes. *Nano Lett* 2022; **22**: 5810–7.
76. Yan JQ. Perspective—the elusive quantum anomalous Hall effect in MnBi_2Te_4 materials. *ECS J Solid State Sci Technol* 2022; **11**: 063007.
77. Hou F, Yao Q and Zhou CS *et al.* Te-vacancy-induced surface collapse and reconstruction in antiferromagnetic topological insulator MnBi_2Te_4 . *ACS nano* 2020; **14**: 11262–72.
78. Huang Z, Du MH and Yan J *et al.* Native defects in antiferromagnetic topological insulator MnBi_2Te_4 . *Phys Rev Mater* 2020; **4**: 121202.
79. Yuan Y, Wang X and Li H *et al.* Electronic states and magnetic response of MnBi_2Te_4 by scanning tunneling microscopy and spectroscopy. *Nano Lett* 2020; **20**: 3271–7.
80. Wu X, Li J and Ma XM *et al.* Distinct topological surface states on the two terminations of MnBi_4Te_7 . *Phys Rev X* 2020; **10**: 031013.
81. Liang Z, Luo A and Shi M *et al.* Mapping Dirac fermions in the intrinsic antiferromagnetic topological insulators $(\text{MnBi}_2\text{Te}_4)(\text{Bi}_2\text{Te}_3)_n$ ($n = 0, 1$). *Phys Rev B* 2020; **102**: 161115.
82. Liu Y, Wang LL and Zheng Q *et al.* Site mixing for engineering magnetic topological insulators. *Phys Rev X* 2021; **11**: 021033.
83. Lai Y, Ke L and Yan J *et al.* Defect-driven ferrimagnetism and hidden magnetization in MnBi_2Te_4 . *Phys Rev B* 2021; **103**: 184429.
84. Riberolles SXM, Zhang Q and Gordon E *et al.* Evolution of magnetic interactions in Sb-substituted MnBi_2Te_4 . *Phys Rev B* 2021; **104**: 064401.
85. Du MH, Yan J and Cooper VR *et al.* Tuning Fermi levels in intrinsic antiferromagnetic topological insulators MnBi_2Te_4 and MnBi_4Te_7 by defect engineering and chemical doping. *Adv Funct Mater* 2021; **31**: 2006516.
86. Garnica M, Otrokov MM and Aguilar PC *et al.* Native point defects and their implications for the Dirac point gap at MnBi_2Te_4 (0001). *npj Quantum Mater* 2022; **7**: 1–9.

87. Chen K, Wang B and Yan JQ *et al.* Suppression of the antiferromagnetic metallic state in the pressurized MnBi_2Te_4 single crystal. *Phys Rev Mater* 2019; **3**: 094201.
88. Chen B, Wang D and Jiang Z *et al.* Coexistence of ferromagnetism and topology by charge carrier engineering in the intrinsic magnetic topological insulator MnBi_4Te_7 . *Phys Rev B* 2021; **104**: 075134.
89. Xie H, Fei F and Fang F *et al.* Charge carrier mediation and ferromagnetism induced in $\text{MnBi}_6\text{Te}_{10}$ magnetic topological insulators by antimony doping. *J Phys D* 2021; **55**: 104002.
90. Murakami T, Nambu Y and Koretsune T *et al.* Realization of interlayer ferromagnetic interaction in MnSb_2Te_4 toward the magnetic Weyl semimetal state. *Phys Rev B* 2019; **100**: 195103.
91. Chen Y, Chuang YW and Lee SH *et al.* Ferromagnetism in van der Waals compound $\text{MnSb}_{1.8}\text{Bi}_{0.2}\text{Te}_4$. *Phys Rev Mater* 2020; **4**: 064411.
92. Shi G, Zhang M and Yan D *et al.* Anomalous Hall effect in layered ferrimagnet MnSb_2Te_4 . *Chin Phys Lett* 2020; **37**: 047301.
93. Ge W, Sass PM and Yan J *et al.* Direct evidence of ferromagnetism in MnSb_2Te_4 . *Phys Rev B* 2021; **103**: 134403.
94. Wimmer S, Sánchez-Barriga J and Küppers P *et al.* Mn-rich MnSb_2Te_4 : a topological insulator with magnetic gap closing at high Curie temperatures of 45–50 K. *Adv Mater* 2021; **33**: 2102935.
95. Chong SK, Lei C and Lee SH *et al.* Anomalous Landau quantization in intrinsic magnetic topological insulators. *Nat Commun* 2023; **14**: 4805.
96. Alexandradinata A, Wang C and Duan W *et al.* Revealing the topology of Fermi-surface wave functions from magnetic quantum oscillations. *Phys Rev X* 2018; **8**: 011027.
97. Jiang Q, Wang C and Malinowski P *et al.* Quantum oscillations in the field-induced ferromagnetic state of $\text{MnBi}_{2-x}\text{Sb}_x\text{Te}_4$. *Phys Rev B* 2021; **103**: 205111.
98. Zyuzin AA and Tiwari RP. Intrinsic anomalous Hall effect in type-II Weyl semimetals. *JETP Lett* 2016; **103**: 717–22.
99. Huan S, Zhang S and Jiang Z *et al.* Multiple magnetic topological phases in bulk van der Waals crystal MnSb_4Te_7 . *Phys Rev Lett* 2021; **126**: 246601.
100. Pei C, Xia Y and Wu J *et al.* Pressure-induced topological and structural phase transitions in an antiferromagnetic topological insulator. *Chin Phys Lett* 2020; **37**: 066401.
101. Shao J, Liu Y and Zeng M *et al.* Pressure-tuned intralayer exchange in superlattice-like $\text{MnBi}_2\text{Te}_4/(\text{Bi}_2\text{Te}_3)_n$ topological insulators. *Nano Lett* 2021; **21**: 5874–80.
102. Yin Y, Ma X and Yan D *et al.* Pressure-driven electronic and structural phase transition in intrinsic magnetic topological insulator MnSb_2Te_4 . *Phys Rev B* 2021; **104**: 174114.
103. Pei C, Xi M and Wang Q *et al.* Pressure-induced superconductivity in magnetic topological insulator candidate MnSb_4Te_7 . *Phys Rev Mater* 2022; **6**: L101801.
104. Ereameev SV, Otrokov MM and Chulkov EV. New universal type of interface in the magnetic insulator/topological insulator heterostructures. *Nano Lett* 2018; **18**: 6521–9.
105. Cao L, Han S and Lv YY *et al.* Growth and characterization of the dynamical axion insulator candidate $\text{Mn}_2\text{Bi}_2\text{Te}_5$ with intrinsic antiferromagnetism. *Phys Rev B* 2021; **104**: 054421.